Acta Cryst. (1981). A37, 273–280

The Ultrastructure of Pyroxenoid Chain Silicates. II. Direct Structure Imaging of the Minerals Rhodonite and Wollastonite

BY DAVID J. SMITH

High Resolution Electron Microscope, Department of Engineering, Free School Lane, Cambridge CB2 3RQ, England

AND D. A. JEFFERSON AND L. G. MALLINSON

Department of Physical Chemistry, Lensfield Road, Cambridge CB2 1EP, England

(*Received* 20 *May* 1980; *accepted* 4 *December* 1980)

Abstract

The feasibility of direct structure imaging of pyroxenoid chain silicates by high-resolution electron microscopy at 500 kV is demonstrated both experimentally and theoretically for the minerals wollastonite, $CaSiO_3$, and rhodonite, $MnSiO_3$. Image simulations with a simplified multi-slice approach indicated that the crystal projection most suitable for direct observation of the tetrahedral chain arrangement corresponded to the overlap of the metal cations with the tetrahedral sites, a situation which occurs in all pyroxenoids. Electron micrographs were also obtained, with bright-field axial illumination at 500 kV, which could be closely matched with the simulated images, at least for very thin crystal regions. The implications of these results, in particular for studies at the atomic level of solid-state transformations involving the pyroxenoids, are briefly discussed.

Introduction

Recent studies of certain members of the pyroxenoid family of minerals by X-ray diffraction and high-resolution electron microscopy (Aikawa, 1979; Jefferson, Pugh, Alario-Franco, Mallinson, Millward & Thomas, 1980) have confirmed that this group of single-chain silicates constitutes a system with a basic structure which may, in principle, be adapted in an almost limitless number of ways to accommodate different conditions of pressure, temperature and chemical substitution (Liebau, 1972; Ohashi & Finger, 1975). Although simple displacement stacking faults in wollastonite, a member of the pyroxenoid group, have previously been the subject of quantitative X-ray diffraction studies (Jefferson & Bown, 1973), such phenomena are best investigated by electron microscopy (Jefferson & Thomas, 1975) where, because the stacking disorder involves only the displacement of individual unit cells, moderate resolution (*ca* 5 Å) is required. Electron-microscopic images of this type consist simply of fringes, the contrast of which bears no straightforward relationship to the detailed atomic structure of the crystals under observation. Nevertheless, shifts of complete unit cells are manifest in the corresponding fringe shifts, and alterations in structural periodicity are also displayed in the fringe periodicity. For such studies, this level of resolution is adequate.

When intimate intergrowths involving variations of structural type within the pyroxenoid group of silicates occur, local variations in the *detailed* atomic structure within any one crystal are commonplace. Systems involving intergrowths of this type are not amenable to quantitative X-ray studies, and even the level of electron-microscope resolution described above is insufficient. Since variations within pyroxenoids often involve an alteration in the repeat length of the silicate chain, corresponding variations in fringe periodicities can usually be observed in simple lattice images. With these images, it has proved possible to investigate such intergrowths in rhodonite (Jefferson *et al.*, 1980), where these are of a relatively simple type. Nevertheless, where intergrowths are of complicated form, such as those involving alterations from the chain-silicate pyroxenoids to the ring-type metasilicates, higher resolution is required since it is necessary to image individual atomic sites for unambiguous image interpretation. We describe here a preliminary investigation of the feasibility of obtaining adequate images of the pyroxenoids by high-voltage, high-resolution electron microscopy for the *direct* structure imaging of the minerals wollastonite and rhodonite.

Experimental

In previous studies of pyroxenoids with the electron microscope it has not been possible to identify the nature of defect structures unambiguously because of insufficient resolution since, for complete elucidation of defects in pyroxenoids, resolutions of the order of 2·5–3·0 Å are required. Taking the interpretable resolution limit of an electron microscope as the first

0567-7394/81/030273-08$01.00

zero of the contrast transfer function (CTF) of the objective lens at, or near, the Scherzer defocus (Erikson & Klug, 1971), commercially available 100 kV electron microscopes with conventional goniometer stages have a limit of around 3·5 Å, although recently this has been pushed to 2·9 Å with a very strong objective lens ($C_s \simeq$ 0·7 mm) and a special goniometer holder (Bursill & Wood, 1978). Direct interpretation of defects in oxides with corner-sharing octahedra is then possible (*e.g.* Iijima & Allpress, 1974; Iijima, Kimura & Goto, 1974) but not where edge sharing of octahedra occurs, as in pyroxenoids.

The recent construction of microscopes operating at higher accelerating voltages, which have been designed specifically for higher-resolution performance, has significantly increased the available interpretable resolution and hence greatly expanded the range of materials for which direct structure projection images can be obtained (*e.g.* Horiuchi, Matsui, Bando, Katsuta & Matsui, 1978; Hutchison, 1979). In particular, the Cambridge University 600 kV high-resolution electron microscope (HREM) (Nixon, Ahmed, Catto, Cleaver, Smith, Timbs, Turner & Ross, 1977; Cosslett, 1980) has recently demonstrated a limit of interpretable resolution approaching 2 Å (Cosslett *et al.*, 1979). Its theoretical CTF is illustrated in Fig. 1, and compared with that obtained experimentally with a Siemens 102, operated at 100 kV (Saxton, Howie, Mistry & Pitt, 1977). This particular instrument, fitted with a 30°, double-tilt, goniometer stage, has been used for this initial study of the pyroxenoid minerals rhodonite and wollastonite. Preliminary results (Jefferson, Thomas, Smith, Camps, Catto & Cleaver, 1979) have already been shown to match closely with previously computed images of wollastonite (Thomas & Jefferson, 1978).

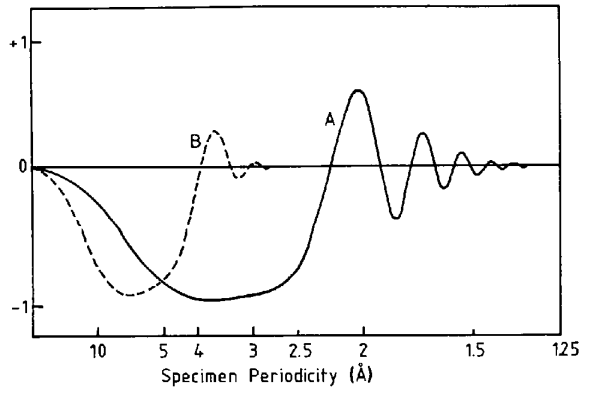

Fig. 1. Theoretical contrast transfer functions, at Scherzer defocus, for (*A*) Cambridge University high-resolution electron microscope, at 500 kV ($C_c = C_s = 3·3$ mm), and (*B*) Siemens 102 at 100 kV ($C_s = 1·8$ mm, $C_c = 2·0$ mm). Each curve includes the effect of finite beam divergence (spatial coherence) and beam energy spread (temporal coherence).

Specimens have been prepared in the usual manner by grinding them in an agate mortar and mounting them on holey carbon films. Image astigmatism was corrected by direct observation of the granularity of the carbon support film at typical magnifications of 500 000 to 600 000 times. However, images were normally recorded at magnifications of 300 000 to 330 000 times (at an accelerating voltage of 500 kV), since the increased resolution of photographic emulsion at higher voltage means that its grain size is not a limiting factor (Camps & Cosslett, 1975).

Image calculations

In an electron-optical investigation of this type, a number of factors will affect image contrast strongly. Interpretable resolution is obviously the main criterion, but the effects of increasing specimen thickness, and the resulting variations in contrast arising from multiple scattering, are important. To investigate the effect of the latter, images were computer simulated with the multi-slice method (Cowley & Moodie, 1957; Goodman & Moodie, 1974) for both rhodonite and wollastonite, for comparison with the experimental images. These calculations were performed on an IBM 370 computer with programs written by one of us (DAJ), for specimen thicknesses ranging from 2·5 to 250 Å, with a slice thickness of 2·5 Å, and for an accelerating voltage of 500 kV, with a spherical aberration coefficient (C_s) of 3·6 mm. The maximum number of beams included in the calculations was 169 for wollastonite and 195 for rhodonite. It was found that chromatic aberration and divergence of the illumination system had little effect on the comparison of experimental and computer images, at least for very thin crystal regions. Beams lying outside the first zero of the CTF were omitted in later calculations since, experimentally, these were found to be relatively weak and have little influence on the image contrast. However, for thicker regions, it might be expected that close agreement with the experimental images might not be obtained, particularly given the higher resolution required compared to 100 kV imaging. Optical diffraction studies of experimental images from thin crystal regions, where the projected charge density (PCD) approximation (Lynch, Moodie & O'Keefe, 1975) was observed to hold from comparison with computed images, showed that ultimate lattice resolution in the image extended to approximately 1·4 Å at 500 kV, which was better than the interpretable resolution limit.

In addition to such factors as interpretable resolution and the effects of multiple scattering, another factor which can limit interpretation of the image in terms of the detailed atomic structure is the actual magnitude and distribution of its contrast. This is especially important in pyroxenoids where there are no obvious

tunnels in the structure as, for example, occur with the complex oxides. As a consequence, it is necessary to choose carefully an appropriate crystal orientation.

These various aspects of image contrast and interpretability for both wollastonite and rhodonite are illustrated by the simulated images in Figs. 2 to 6. Fig. 2 demonstrates the advantages, with regard to the interpretation of image contrast in terms of atomic detail, which accrue from using the 600 kV instrument rather than a conventional 100 kV machine such as the Siemens 102: the tetrahedral stacking arrangement in wollastonite (normally represented 1.2.1.2.1.2... where the numbers represent tetrahedra pointing in the same direction) is clearly revealed in the [001] axis projection. Fig. 2(*a*) shows the structure potential projected along this direction, three pairs of interlocking chains being clearly displayed. Fig. 2(*b*) shows the corresponding image contrast predicted from a thin phase grating for observation in the Siemens 102 at the Scherzer defocus. Although three pairs of fringes are visible, direct interpretation of the structure in terms of atomic positions is not possible because of insufficient resolution. However, in the simulated 500 kV image, again from a thin phase grating at Scherzer defocus (Fig. 2*c*), correspondence with the projected structure is readily apparent, the tetrahedral repeat being well resolved and the true chain structure being made visible.

In the simulated image of Fig. 2(*c*) it would appear that the tetrahedral chain structure in wollastonite is clearly resolved in the image. Note, however, that it is an oversimplification to state that the tetrahedra are being directly observed since the structure consists of both Ca^{2+} ions and SiO_4 tetrahedra, and one might anticipate that the former will provide the major contribution to the observed image contrast. In effect, the dark blobs in the image of Fig. 2(*c*) represent not merely the SiO_4 tetrahedra alone but the superposition of Ca^{2+} ions and tetrahedra. This is illustrated particularly well in Fig. 3. Figs. 3(*a*) and (*b*) correspond to a projection on to the plane of the octahedral ribbons in wollastonite, this being approximately equivalent to a [101] axis projection. Although the structure is clearly indicated in Fig. 3(*a*), the corresponding projected potential (Fig. 3*b*) provides little evidence of this, because adjacent octahedral ribbons in this projection lie above the gaps between ribbons shown in Fig. 3(*a*), producing, in projection, a near uniform potential. Correspondingly, although images taken with the beam in this direction might be expected to show the chain periodicity, they will not give a detailed picture of the atomic arrangement. However, with the electron beam parallel to [001], as illustrated in Figs. 3(*c*) and (*d*), it

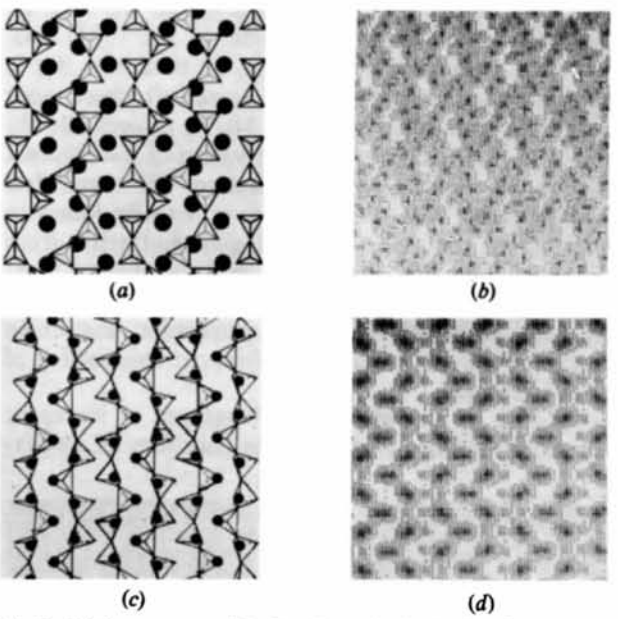

Fig. 3. (*a*) Structure model of wollastonite in the [101] zone-axis projection showing SiO_4 tetrahedra and Ca^{2+} ions (solid circles); (*b*) corresponding projected potential; (*c*) structure model of wollastonite in the [001] zone-axis projection; (*d*) corresponding projected potential.

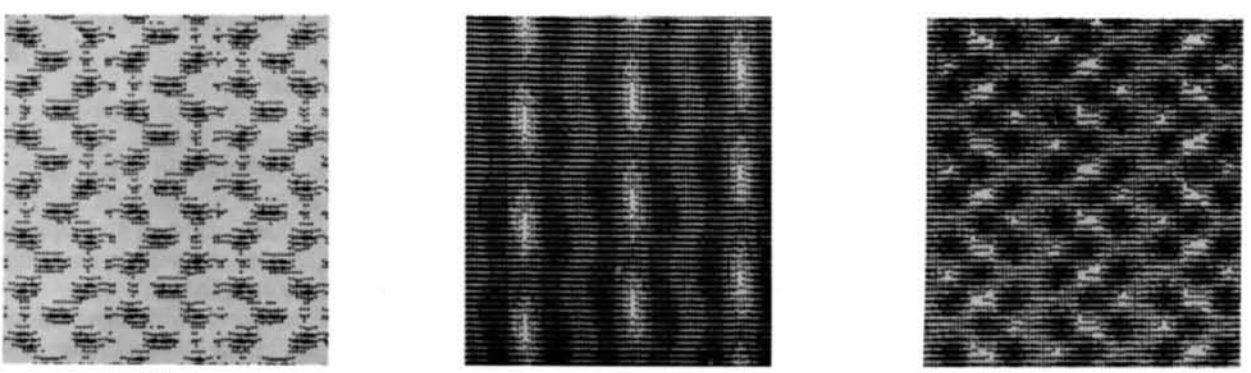

Fig. 2. Image simulations for a thin crystal of wollastonite: (*a*) structure potential projected along the [001] zone axis; (*b*) image of a thin phase grating in this projection at 100 kV and Scherzer defocus; (*c*) corresponding image at 500 kV and Scherzer defocus.

can be seen that Ca^{2+} ions project almost directly above the SiO_4 tetrahedra: the combination of these two features produces a distinct maximum in the projected potential and, correspondingly, a dark patch in the image contrast. In this latter projection, therefore, we effectively view the chain arrangement by observing the Ca^{2+} ions in the octahedral ribbon: it is only in this projection that the positions of these ions mimic the positions of SiO_4 tetrahedra and consequently, for direct observation of the tetrahedral chain arrangement, this is the only structural projection suitable.

A similar situation is found in rhodonite, as shown in Fig. 4. Here again the projection on to the plane of the octahedral ribbons ([100] axis projection) gives a relatively flat projected potential (Figs. 4*a* and *b*). However, an equivalent direction to the [001] projection in wollastonite also exists. In rhodonite this is the [1$\bar{1}$0] axis projection (Figs. 4*c* and *d*) where, once again, the cations (in this case Mn^{2+}) project directly above the SiO_4 tetrahedra: observation of the contrast due to these cations also emphasizes the tetrahedral configuration. This characteristic is actually found to occur in all the single-chain silicates, and arises from the fact that the tetrahedral and octahedral configurations are interdependent. Consequently, by utilizing this particular structural projection, the chain configuration can be directly observed irrespective of its periodicity.

As well as indicating the advantages of increased resolution and demonstrating the feasibility of observing the chain configuration of these silicates directly, simple image simulations of this type also show some of the possible drawbacks. Fig. 5 for example shows the variations of image contrast at Scherzer defocus for both (*a*) wollastonite and (*b*) rhodonite, as a function of crystal thickness. In both materials, the correspondence between regions of dark image contrast and maxima in the projected potential is apparent at a thickness of 25 Å, whereas, for a thickness of only 50 Å, this close correspondence is already lost. Although the image for a thickness of 25 Å appears to return, albeit with reversed contrast, by the time the specimen thickness has reached 100 Å, further increases in thickness result in images which, although showing considerable fine detail, bear no resemblance to the actual crystal structure. This suggests, therefore, that the direct structural interpretation of pyroxenoid images at high voltage, and increased resolution, requires specimen thicknesses of not much greater than 25 Å, which represents a more severe requirement than that imposed for direct structure imaging at 100 kV and resolutions greater than 3·5–4·0 Å. This restriction is discussed further below.

As might be anticipated from image simulations and observations at 100 kV, variation in the objective-lens defocus also has an important influence on image contrast, even when the specimen thickness is such that 1 : 1 correspondence between image and object *may* be achieved near the optimum defocus. This is illustrated in Fig. 6 for a crystal of wollastonite of 25 Å thickness. Only over the approximate focal range from 700 to 900 Å underfocus (*i.e.* around Scherzer defocus) is the image contrast closely representative of the projected structure. Outside this region, fine image detail remains but is not interpretable in terms of the crystal structure: the pairs of chains are no longer clearly resolved. Finally, it is interesting to observe (see below) that image contrast may be reversed completely at positions above Gaussian focus, a not uncommon situation which can occur when the diffracted beams primarily responsible for the image contrast lie within a relatively small range of spatial frequencies, but which is unlikely when any structural disorder is present.

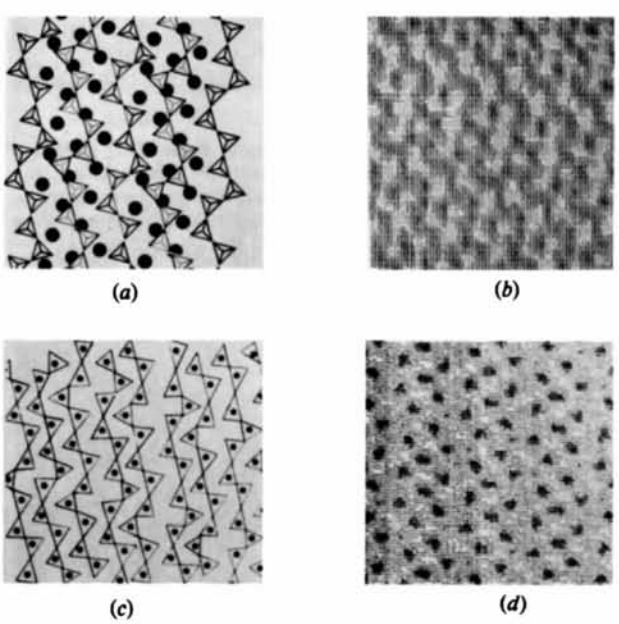

Fig. 4. (*a*) Structure model of rhodonite in the [100] zone-axis projection showing SiO_4 tetrahedra and Mn^{2+} ions (solid circles); (*b*) corresponding projected potential; (*c*) structure model of rhodonite in the [110] zone-axis projection; (*d*) corresponding projected potential.

Results

Our computer simulation studies suggest that quite stringent conditions need to be fulfilled in order that the direct imaging of the structure of single-chain silicates will be successful. Although these might, at first, appear too severe, we have been able to show experimentally that they can, nevertheless, be satisfied.

Obtaining crystals close to the required orientations proved relatively easy for both wollastonite and rhodonite. The former mineral, which normally exhibits considerable stacking disorder (Jefferson & Thomas, 1975), proved easy to recognize, and to orient, due to

the diffuse streaks in the diffraction pattern which lie in the (*hk*0) section. Greater difficulty was experienced with rhodonite, where no stacking disorder was present to any great extent, since several of the reciprocal-lattice sections appear quite similar on initial examination. Nevertheless, several crystals were eventually tilted to the correct zone-axis orientation. One image feature, common to both minerals, was an apparent buckling along the thin crystal edges, over relatively short distances. Frequent small corrections of crystal tilt were necessary, using selected-area diffraction patterns from very small regions, to ensure that the required axis remained parallel to the electron beam

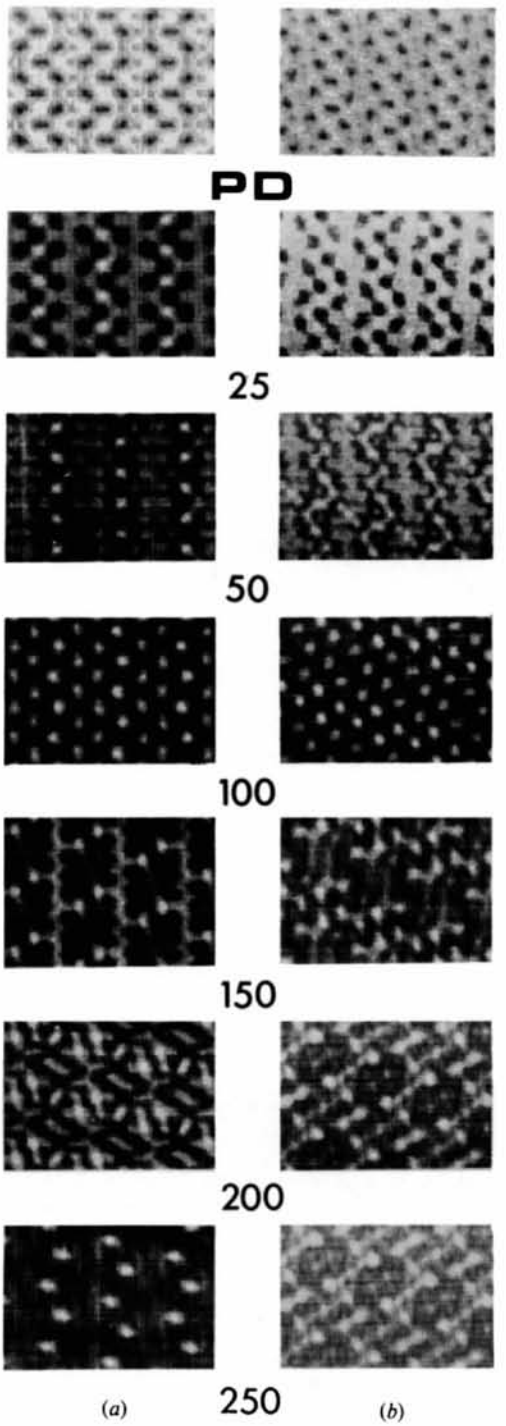

Fig. 5. Simulated variation of contrast at Scherzer defocus with increasing crystal thickness, as indicated, together with respective projected potentials: (*a*) wollastonite in [001]; (*b*) rhodonite in [1$\bar{1}$0].

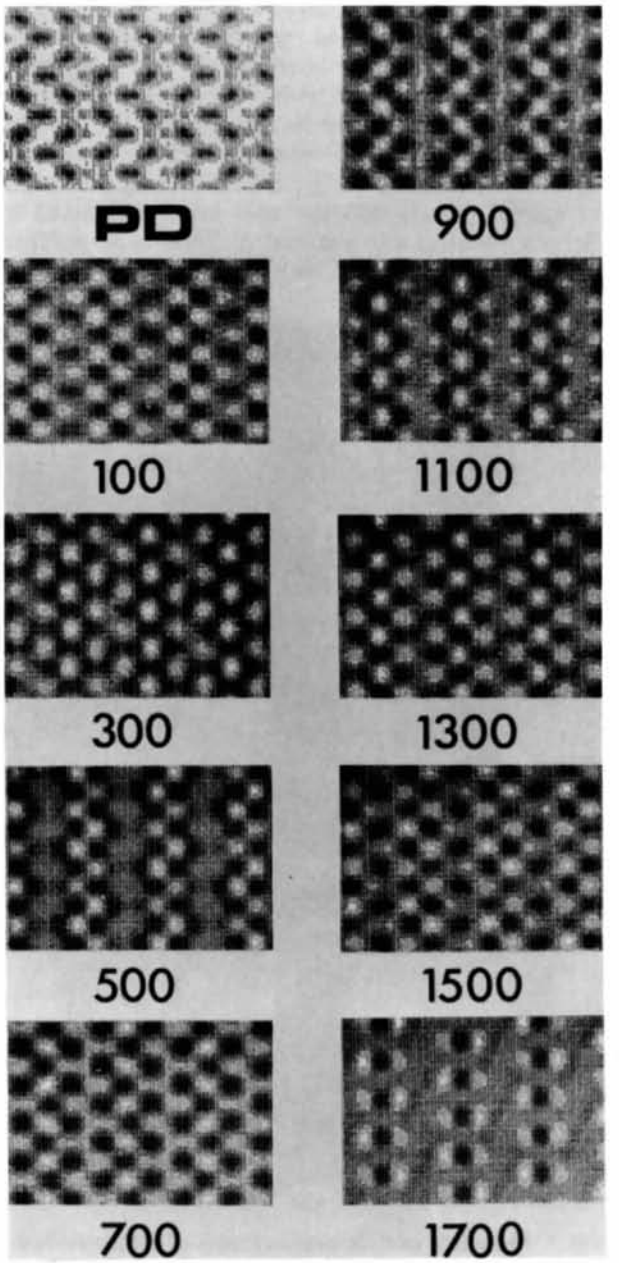

Fig. 6. Simulated variation of contrast with change of focus for a wollastonite crystal of 25 Å thickness in the [001] zone-axis projection.

because of the extreme sensitivity of the images to slight changes in crystal orientation.

Some typical images of wollastonite, taken with the electron beam parallel to [001], are shown in Fig. 7. The edge of a relatively thick crystal is shown in Fig. 7(*a*). It appears to have a layer of amorphous material along its edge, as well as showing considerable stacking disorder in the thicker region. Although most of the crystal is too thick for direct correspondence between the image and the actual structure, the image near the edge matches very clearly with the contrast computed for a crystal of 25 Å thickness at Scherzer defocus. Fig. 7(*b*) shows the edge of another crystal together with the simulated image for a (positive) defocus of 100 Å, which matches it closely. There is a complete reversal of contrast from that at the optimum defocus, with the superimposed cation and tetrahedral sites appearing white. Fig. 7(*c*) shows a thicker region of a third crystal with the inset image computed for Scherzer defocus and a crystal thickness of 50 Å. There is reasonable agreement with the coarser experimental image features, namely the larger white blobs, but not of the fine detail.

An image of a crystal of rhodonite in the [1$\bar{1}$0] projection, taken near the optimum defocus, is shown in Fig. 8: several steps of increasing thickness are clearly visible. Reasonable agreement with the simulated image for a crystal thickness of 25 Å is again obtained near the edge as shown in the inset (*c*) whereas, at inset (*a*), calculated for a thickness of 150 Å, a broad similarity only is apparent, and at (*b*), calculated for a thickness of 50 Å, the similarity is perhaps even less. The rapid change in appearance of the image with thickness, and the increasingly finer detail visible in the thicker regions, again emphasizes the importance of dynamical scattering in practice, and indicates that any interpretation of structural defects in the pyroxenoids at this level of resolution will be fraught with pitfalls in any but the thinnest of crystals, at least without much more comprehensive calculations than we have employed here. It should also be remarked that, for all the crystals of rhodonite

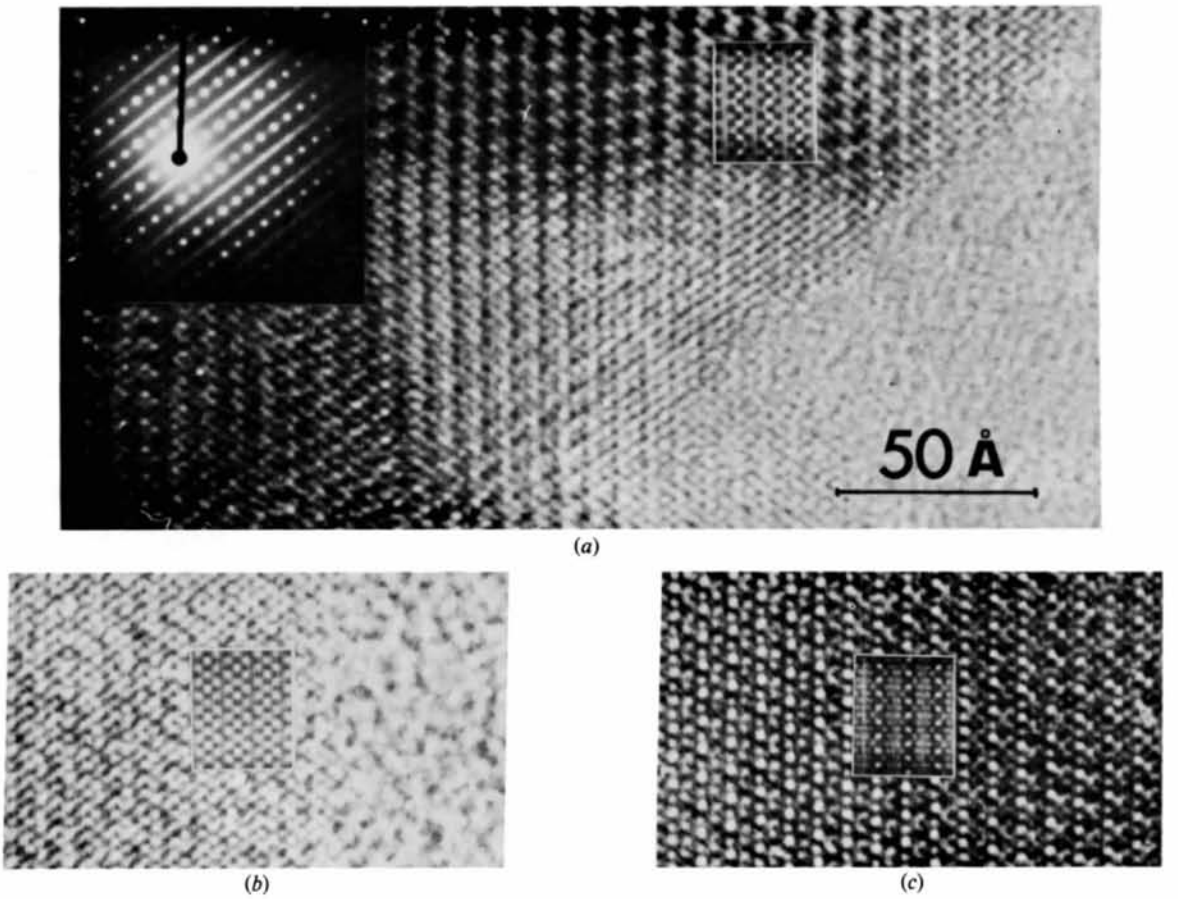

Fig. 7. Bright-field axial-illumination images of wollastonite in the [001] zone-axis projection taken at 500 kV: (*a*) near a crystal edge, and including the simulated image at Scherzer defocus for a crystal of 25 Å thickness and the corresponding electron diffraction pattern for this crystal projection; (*b*) near the edge of another crystal, together with the simulated image for 100 Å (positive) defocus; note the contrast reversal from that at Scherzer defocus; (*c*) a slightly thicker crystal region, together with the simulated image at Scherzer defocus for a thickness of 50 Å.

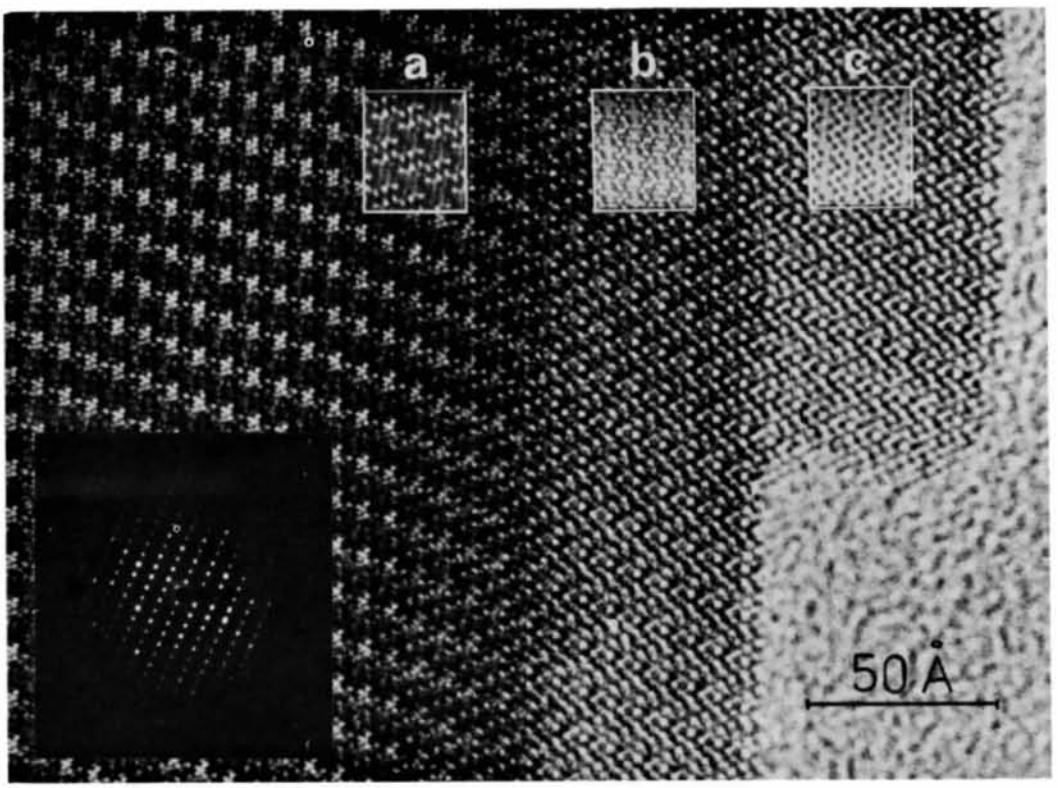

Fig. 8. Bright-field axial-illumination image of rhodonite in the [110] zone-axis projection, as shown in the electron diffraction pattern, recorded at 500 kV close to Scherzer defocus. The inset simulated images are calculated for crystal thicknesses of (*a*) 150 Å, (*b*) 50 Å and (*c*) 25 Å.

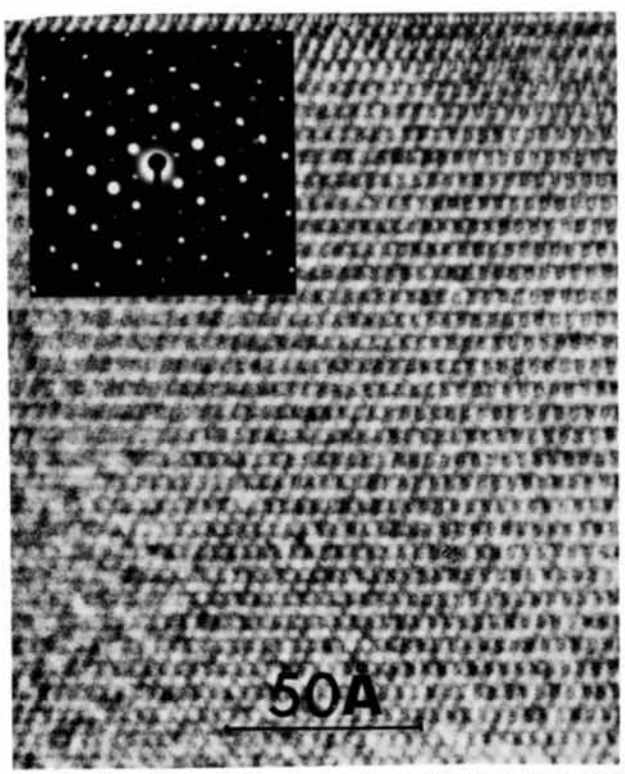

Fig. 9. Bright-field axial-illumination image of wollastonite recorded at 500 kV, in an alternate zone-axis projection, as shown in the electron diffraction pattern inset.

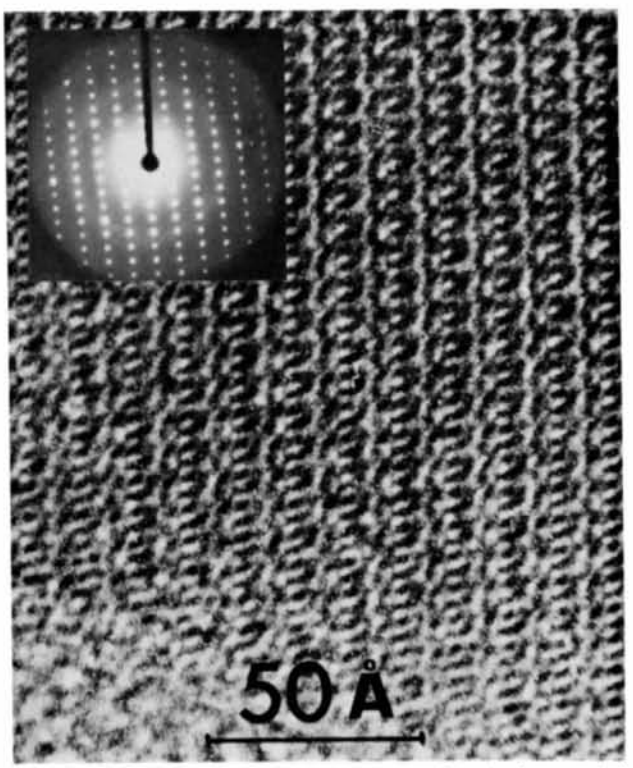

Fig. 10. Bright-field axial-illumination image of rhodonite recorded at 500 kV, in the [110] zone-axis projection, as shown in the electron diffraction pattern inset.

observed, and similarly for wollastonite, only very narrow strips at the crystal edges showed the intensity distribution expected of the structure projection image.

Finally, for completeness, we include experimental images of both wollastonite (Fig. 9) and rhodonite (Fig. 10) in alternate zone-axis projections. Matching image simulations are not provided since, as discussed above, the overlapping of the octahedral ribbons with the tetrahedral chains precludes delineation of the actual chain arrangement.

Discussion

We have been successful in the primary objective of the present study which was to establish the feasibility of direct structure imaging in pyroxenoid chain silicates with high-resolution electron microscopy at high voltage. Appropriate crystal projections, namely those corresponding to overlap of the metal cation positions with the tetrahedral sites, were indicated by image simulations, and experimental images were also obtained at 500 kV which matched closely with those simulated for very thin crystal regions. However, it is of considerable concern, given our long-term objectives of imaging, and interpreting, isolated structural defects at the atomic level in the pyroxenoids, as outlined here and elsewhere (Thomas, Jefferson, Mallinson, Smith & Crawford, 1979; Jefferson *et al.*, 1980), that both the simulated and experimental images displayed such rapid variations in contrast with increasing crystal thickness, and that agreement between computation and experiment also appeared to worsen rapidly with thickness. Admittedly, more extensive calculations could be undertaken, in particular to ensure that sufficient diffracted beams were included to obtain a closer fit with the higher-resolution detail, especially at greater thicknesses. Furthermore, it should be noted that, although it is expected that the crystal thicknesses which can be tolerated for structure projection images increase with accelerating voltage (*e.g.* Bursill & Wood, 1978), it is nevertheless well established that image contrast for a given crystal thickness may vary drastically depending on the intensities and phases of the beams transmitted by the objective aperture (*e.g.* Allpress & Sanders, 1973). Further studies are in progress, both experimental and computational, to investigate these various possibilities, such as the effect of accelerating voltage and objective aperture size, in order that the optimal conditions for imaging structural defects in the pyroxenoids can be determined.

The Cambridge University 600 kV high-resolution electron microscope has been constructed as a joint project between the Cavendish Laboratory and the Department of Engineering, with major financial support from the Science Research Council, to whom DJS and LGM are also grateful for personal support.

We are also pleased to acknowledge the interest and encouragement of Professor J. M. Thomas, FRS.

References

AIKAWA, N. (1979). *Mineral. J. Jpn*, **9**, 255–269.

ALLPRESS, J G. & SANDERS, J. V. (1973). *J. Appl. Cryst.* **6**, 165–190.

BURSILL, L. A. & WOOD, G. J. (1978). *Philos. Mag.* **38**, 673–689.

CAMPS, R. A. & COSSLETT, V. E. (1975). *Microscopie Electronique à Haute Tension*, edited by B. JOUFFREY & P. FAVARD, pp. 71–74. Paris: Societé Francaise de Microscopie Electronique.

COSSLETT, V. E. (1980). *Proc. R. Soc. London Ser. A*, **370**, 1–16.

COSSLETT, V. E., CAMPS, R. A., SAXTON, W. O., SMITH, D. J., NIXON, W. C., AHMED, H., CATTO, C. J. D., CLEAVER, J. R. A., SMITH, K. C. A., TIMBS, A. E., TURNER, P. W. & ROSS, P. M. (1979). *Nature (London)*, **281**, 49–51.

COWLEY, J. M. & MOODIE, A. F. (1957). *Acta Cryst.* **10**, 609–619.

ERIKSON, H. P. & KLUG, A. (1971). *Philos. Trans. R. Soc. London Ser. B*, **261**, 105–118.

GOODMAN, P. & MOODIE, A. F. (1974). *Acta Cryst.* A**30**, 280–290.

HORIUCHI, S., MATSUI, Y., BANDO, Y., KATSUTA, T. & MATSUI, I. (1978). *J. Electron Microsc.* **27**, 39–46.

HUTCHISON, J. L. (1979). *Chem. Scr.* **14**, 181–186.

IIJIMA, S. & ALLPRESS, J. G. (1974). *Acta Cryst.* A**30**, 29–36.

IIJIMA, S., KIMURA, S. & GOTO, M. (1974). *Acta Cryst.* A**30**, 251–257.

JEFFERSON, D. A. & BOWN, M. G. (1973). *Nature (London)*, **245**, 43–44.

JEFFERSON, D. A., PUGH, N. J., ALARIO-FRANCO, M., MALLINSON, L. G., MILLWARD, G. R. & THOMAS, J. M. (1980). *Acta Cryst.* A**36**, 1058–1065.

JEFFERSON, D. A. & THOMAS, J. M. (1975). *Mater. Res. Bull.* **10**, 761–765.

JEFFERSON, D. A., THOMAS, J. M., SMITH, D. J., CAMPS, R. A., CATTO, C. J. D. & CLEAVER, J. R. A. (1979). *Nature (London)*, **281**, 51–53.

LIEBAU, F. (1972). *Handbook of Geochemistry*, Vol. II, Ch. 14. Berlin: Springer-Verlag.

LYNCH, D. F., MOODIE, A. F. & O'KEEFE, M. A. (1975). *Acta Cryst.* A**31**, 300–307.

NIXON, W. C., AHMED, H., CATTO, C. J. D., CLEAVER, J. R. A., SMITH, K. C. A., TIMBS, A. E., TURNER, P. W. & ROSS, P. M. (1977). In *Electron Microscopy and Analysis* 1977, edited by D. L. MISELL, pp. 13–16. Bristol and London: Institute of Physics.

OHASHI, Y. & FINGER, L. W. (1975). *Ann. Rep. Carnegie Inst. Washington*, **74**, 564–569.

SAXTON, W. O., HOWIE, A., MISTRY, A. & PITT, A. J. (1977). In *Electron Microscopy and Analysis* 1977, edited by D. L. MISELL, pp. 119–122. Bristol and London: Institute of Physics.

THOMAS, J. M. & JEFFERSON, D. A. (1978). *Endeavour*, **2**, 127–136.

THOMAS, J. M., JEFFERSON, D. A., MALLINSON, L. G., SMITH, D. J. & CRAWFORD, E. S. (1979). *Chem. Scr.* **14**, 167–179.